ACOUSTO-OPTIC GYROSCOPE

Ashraf Mahmoud[*†], *Mohamed Mahmoud*[†], *Lutong Cai*[†], *MSI Khan, James A. Bain, Tamal Mukherjee, and Gianluca Piazza*
Carnegie Mellon University, Pittsburgh, PA, USA

ABSTRACT

An Acousto-Optic Gyroscope (AOG) consisting of a Mach-Zehnder interferometer (MZI) embedded into two inherently matched piezoelectric SAW resonators sharing the same cavity is presented. This constitutes the first demonstration of a MEMS strain-based optomechanical gyroscope that uses refractive index change due to the acousto-optic effect rather than conventional displacement sensing. This first prototype integrates acoustic and photonic components on the same lithium niobate on insulator (LNOI) substrate and showcases how optical detection can provide greater stability compared to acousto-electric transduction. This approach enables the development of a new class of MEMS-based gyroscopes that combines the advantages of both conventional MEMS and optical gyroscopes.

INTRODUCTION

Existing gyroscopes for inertial navigation systems are based on either bulky mechanical implementations [1] or large volume Optical Gyroscopes (OGs) [2]. MEMS vibratory gyroscopes (MVG) are an interesting alternative, but have exhibited limitations on various fronts. The need for a large released mass makes the MVG vulnerable to shock [3]. Since most MVGs operate at few kHz with quality factors > 1000, their output bandwidth is limited to mHz for frequency matched operation [4] unless complex bandwidth extension techniques are used [5]. Furthermore, the low operation frequency makes the gyroscope susceptible to environmental vibrations [6]. On the other hand, OGs such as Fiber Optic Gyroscope (FOG) and Ring Laser Gyroscope (RLG) can achieve both high performance and operation stability [2]. Unfortunately, miniaturization and power scaling of these implementations are challenging. In this work, we demonstrate the first prototype of an Acousto-Optic Gyroscope (AOG), which is capable of addressing all the major issues encountered in MVG or miniaturized OGs. The AOG is based on the concept of the Surface Acoustic Wave Gyroscope (SAWG) [7], in which the Coriolis force detection is performed optically instead of acousto-electrically. The use of SAW resonators enables the realization of a large unreleased mass. The optical sensing can provide extremely low noise levels and stable readout. In addition, the optical modulation method significantly simplifies the electronic readout.

PRINCIPLE OF OPERATION

Figure 1 depicts a schematic view of the structure and offers an overview of the principle of operation of the AOG. Two orthogonal SAW resonators are shown with metallic pillars placed at the center acting as the moving mass, M_p, of the gyroscope. A SAW standing wave pattern is established along the x (drive) direction. The pillars are placed inside the cavity at the anti-nodes of the SAW standing wave pattern (max x-directed velocity). The pillars are driven longitudinally with vibration velocity, v_p. When out-plane rotation, Ω_z, is applied, Coriolis force, F, is induced on the vibrating pillars in the direction orthogonal to both the input rotation direction and the drive vibration direction and can be expressed as:

$$F = -2M_p\Omega_z \times v_p \quad (1)$$

The pillars are arranged in a checkerboard configuration such that constructive interference for a secondary SAW wave is established in the y (sense) direction. The strain value, S, associated with this wave can be expressed in terms of the Coriolis force, F, the substrate mass density, ($\rho = 4700 kg/m^3$) for LN, the Rayleigh SAW phase velocity, ($v_R = 3488 m/\sec$), the SAW penetration depth, H (which is around 10% of the acoustic wavelength Λ), and the acousto-optical (AO) interaction length, L, as:

$$S = \frac{F}{\rho v_R^2 LH} \quad (2)$$

In SAW gyroscopes, piezoelectric transducers are commonly used to sense the secondary waves. In this work, the secondary wave is detected through the elasto-optic effect by the photonic waveguides etched in the Lithium Niobate (LN) thin film, *i.e.* by monitoring the refractive index change, Δn, due to the stress, S:

$$\Delta n = \frac{1}{2} n^3 p_{eff} S \quad (3)$$

where p_{eff} is the effective acousto-optic coefficient in the specific propagation direction of the SAW.

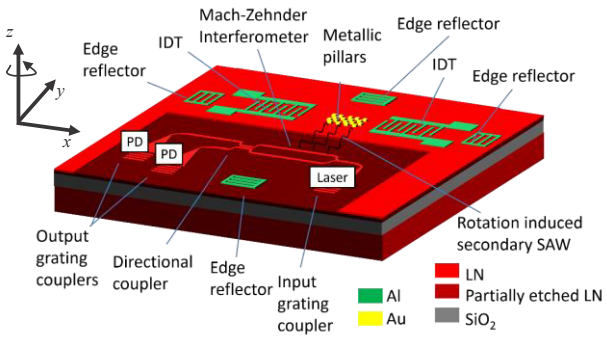

Figure 1: 3D sketch for the AOG. PD=Photo-detector, IDT=Interdigitated transducer.

ACOUSTO-OPTIC GYROSCOPE DESIGN

Figure 2 shows the layout view for the proposed AOG with zoomed-in SEMs of the various components. Four identical Interdigitated Transducers (IDT), SAW reflectors and photonic waveguides are placed symmetrically with respect to a central pillar-filled cavity so as to ensure frequency matching between orthogonal SAW resonators. The photonic readout shown in the same figure is based on

a Mach-Zehnder interferometer (MZI) [8] where the light is coupled in and out using grating couplers. Y junction is used for splitting the optical input into the two arms of the MZI and a 2x2 multimode interference (MMI) 3-dB coupler is used as a beam combiner. The differential output is detected using a balanced photodetector.

AOG Scale Factor and MZI Design

The normalized differential transfer function of the MZI, T_{MZI} can be expressed in terms of the phase shift between the two arms, φ, as $T_{MZI} = \sin\varphi$.

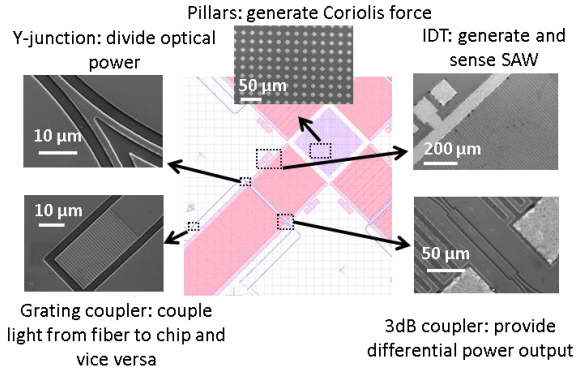

Figure 2: Layout view of the AOG with zoomed-in SEMs of the various components forming it.

Separating the two MZI arms by $3\Lambda/2$ enables push-pull operation, which doubles the phase sensitivity. Additionally, placing the waveguides at the location of maximum strain for the standing wave pattern of the SAW cavity enhances the phase sensitivity by the resonator quality factor in the sense direction, Q_S. This phenomenon is described by:

$$\varphi = 2Q_S \frac{2\pi}{\lambda}\Delta n \qquad (4)$$

where $\lambda = 1550\,nm$ is the optical wavelength.

The vibration velocity in Eq. (1) can be expressed in terms of the drive parameters: the electrical power, P_m, the drive resonator quality factor, Q_D, the resonator equivalent mass, M_r, and the SAW resonance frequency, f_m, as:

$$v_p = \sqrt{\frac{P_m Q_D}{\pi f_m M_r}} \qquad (5)$$

Combining equations (1-5), the AOG Scale Factor (SF) can be expressed as:

$$SF = \left|\frac{\partial T_{MZI}}{\partial \Omega_z}\right|_{\max} = \frac{4\pi}{\lambda H}\sqrt{\frac{M_2}{\rho v_R}}M_P\sqrt{\frac{P_m Q_D}{\pi f_m M_r}}Q_S \qquad (6)$$

where $M_2 = \left(n^6\left(p_{eff}\right)^2\right)/\left(\rho v_R^3\right)$ is the AO figure of merit of the material. The AO interaction length (MZI arms' length) is equal to the the total cavity length and is chosen to be $L = 40\Lambda$. The acoustic wavelength is selected to be $\Lambda = 30\mu m$ so as to fit the gyroscope design in a 20x20 mm^2 die. The lithography resolution limited the width of the waveguide to a value of $2\mu m$, which corresponds to a multi-mode operation. Single-mode operation is not required for the AOG.

SAW Resonator Design

The equation for the SF assumes that the sense and drive resonator are perfectly matched so that the resonator Q in the drive and sense directions can be fully harnessed. Previous SAW gyroscope designs [7], [9] targeted SAW propagation direction and LN wafer cuts that provide the highest electromechanical coupling coefficient such as propagating the SAW in the Z direction for a Y cut LN wafer. However, for such a cut, the material properties in the two orthogonal in-plane directions X and Z are not the same due the trigonal crystalline structure of LN. Such a configuration makes frequency matching difficult. The two SAW resonators in the present AOG are rotated by *+/-45°* with respect to the Z-direction, to preserve symmetry, inherently matching the drive and sense frequency.

To maximize SF, M_P is increased by using a high density material (Au) to form the pillars. To ensure maximum vibration of the moving pillar, the length and width of the pillar is set to be $\Lambda/4$. To make M_p large, thick pillars should be used. However, increasing the thickness of the pillars increases the SAW losses and reduces both Q_D and Q_S. For this reason, the pillar thickness is limited to 140 nm. The cavity area includes a total of 3,200 pillars. To properly confine the SAW inside the acoustic cavity and hence maximize Q_D and Q_S, gratings with high numbers of reflectors (700 finger each side) are used. The number of IDT fingers (N_{pair}=43) is selected to achieve 50 Ω matching. The metallization ratio, $\eta = 50\%$, and pitch, $p = \Lambda/2$, are selected to ensure both the IDT and the reflector center frequencies are matched.

Grating Coupler and MMI Coupler Design

The dimensions of the grating coupler were optimized for maximum coupling efficiency for the TE polarized light using the Finite Difference Time Domain (FDTD) LUMERICAL modeling software. These dimensions are $\Delta_g = 1\mu m$ for the period, $\delta/\Delta_g = 0.44$ for the duty cycle and $e = 330nm$ for the etch depth [10]. The same etch depth was used to define the waveguide thickness as both the coupler and the waveguide are defined during the same etch step. The length and width of the MMI coupler are chosen to be $118.1\mu m$ and $11.6\mu m$, respectively to ensure 3-dB splitting around 1550 nm (optical wavelength).

FABRICATION PROCESS

The fabrication process flow is depicted in Figure 3 starting with a Y-cut LNOI 4'' wafer. The LN thin film (3'' diameter and 500 nm in thickness) was bonded to Silicon dioxide (SiO_2, $1\mu m$ thick) on a LN substrate using the Smart-Cut technology (Figure 3-A) by an external vendor [11]. The first step is the lift-off of evaporated Al thin film (Figure 3-B), which is 100 nm thick. After this step, a 140 nm Au layer lift-off is performed (Figure 3-C) for patterning of the pillars. Au is also used for coating the Al pads to enable wire bonding for testing purposes. The next step is the deposition of SiO_2 (1 µm thick) (Figure 3-D), which is used as a mask layer during the LN etch. Chromium (Cr) (50 nm thick) is then deposited

(Figure 3-E) and used as a mask for etching SiO_2. This Cr layer is patterned twice. The first pattern is done with optical lithography to define the waveguides (WGs) (Figure 3-F). The second Cr patterning is performed at the die level using electron-beam lithography to define the grating couplers (Figure 3-G). Then SiO_2 is etched in an RIE process using fluorine-based chemistry with the twice-defined Cr mask (Figure 3-H). Chlorine-based chemistry is used in an ICP process to partially etch the LN with the SiO_2 mask (Figure 3-I). The Cr mask is also removed during the ICP etch step. The final step is dry etch of SiO_2 to expose the metallic pads.

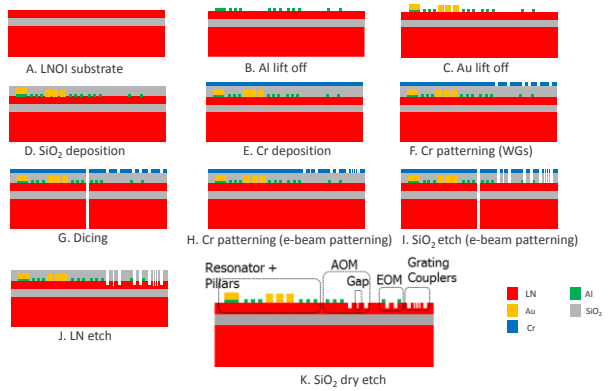

Figure 3: Fabrication process flow for building the AOG.

MEASUREMENT RESULTS

Characterization of SAW resonators

The frequency responses of the drive and sense resonators were measured using a vector network analyzer (PNA N5230A) and RF probing. The measurement results are shown in Figure 4. The ~40 kHz mismatch between sense and drive frequencies can be attributed to fabrication misalignments. This mismatch is still within the resonator bandwidth, which is approximately 100 kHz (loaded $Q_D = Q_S = 1000$).

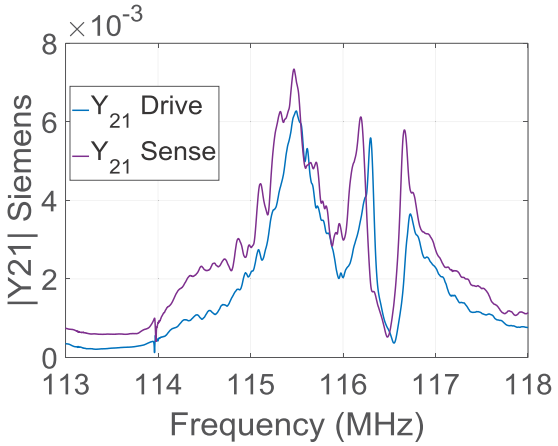

Figure 4: Frequency response for the drive and sense cavities showing a mismatch of 40 kHz.

Characterization of Photonic MZI

Figure 5 plots the MZI transfer function for the two outputs as a function of the wavelength. A balanced output is achieved at a few wavelengths near the design value of 1550 nm. The slight shift in the wavelength might be attributed to differences in the actual dimensions of the etched waveguides with respect to the design values. The envelope reflects the transfer function of the grating couplers.

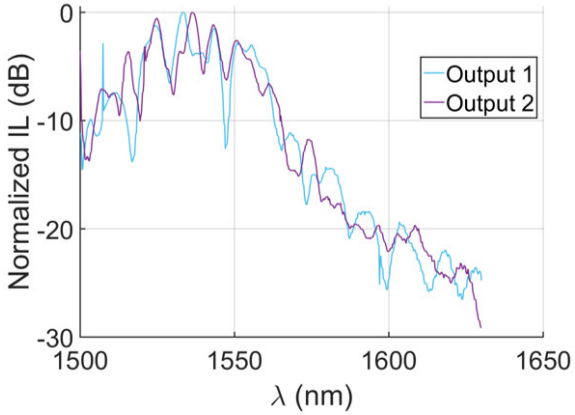

Figure 5: Measured insertion loss for the two output ports of the MZI as function of the wavelength.

Gyroscope Measurement

The AOG measurement setup is shown in Figure 6 where the sample is mounted on the rate table together with the optical positioners and connected to the measurement instruments. The gyroscope die is packaged in a PGA ceramic package. An Ultra-High Frequency Lock-In (UHFLI) amplifier from Zurich Instruments is used to phase lock the SAW drive resonator using a built-in PLL. In addition, a built-in PID controller is used to amplitude-control the drive signal for the SAW resonator

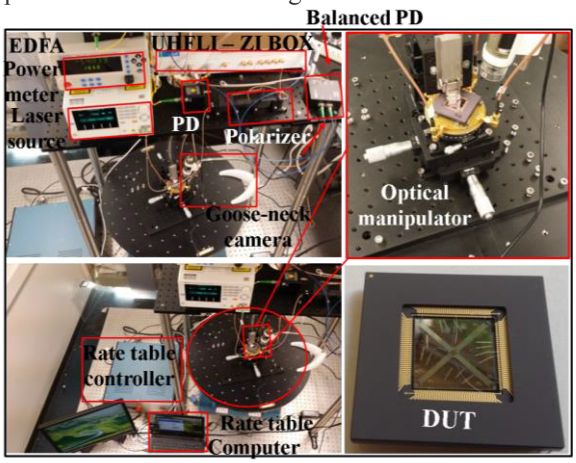

Figure 6: AOG measurement setup. The optical setup with the positioners and manipulators are mounted on top of the rate table.

and reject any variations due to vibration or temperature drift. A tunable laser generated carrier is coupled into the optical grating via a vertical groove array (VGA) which also couples out the modulated gyroscope signal. The optical alignment is optimized by adjusting a six degree of freedom manipulator and sweeping the wavelength. A minimum insertion loss of -27 dB was achieved for this optical transfer function. The photonic output is fed to the lock-in amplifier where the Coriolis component is separated from the quadrature component. Due to the RF connecting cables and fibers, full 360^0 rotations for the rate table are not allowed. Instead, the applied input rotation is a sinusoidal oscillation of fixed frequency (2 Hz) and variable amplitude. Due to the oscillatory motion, induced vibrations affect the VGA and the quality of the optical

alignment to the sensor. Those changes have a direct effect on the scale factor measurements leading to run-to-run variations. The recorded variations in the optical coupling losses are bound within *+/-1.5 dB*. As shown in Figure 8, the measured scale factor is in good agreement with theoretical predictions. The recorded variations in the scale factor are found to be within the theoretically

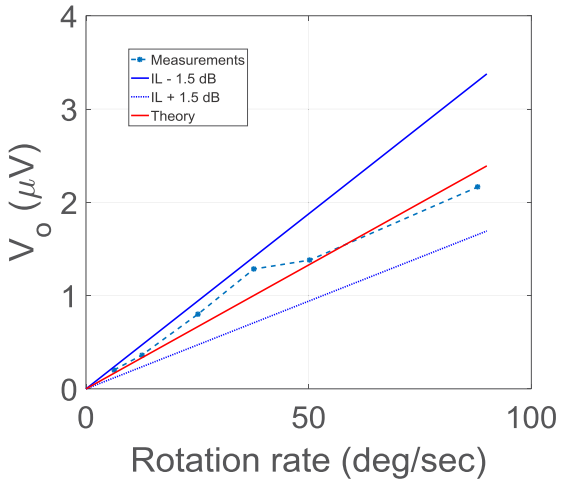

Figure 7: Measured output voltage as a function of rotation rate compared with theory. Margins due to variations in coupling losses (fiber misalignment) are provided as ±1.5 dB.

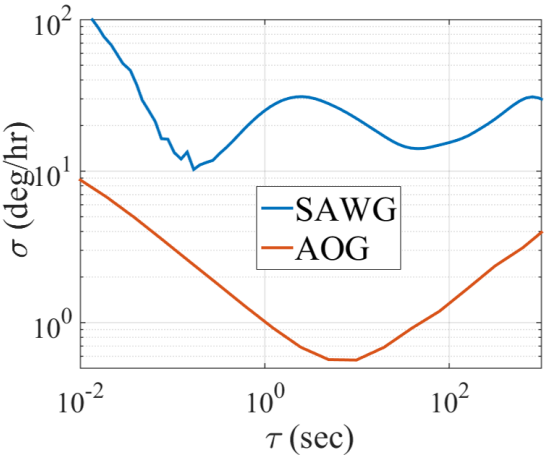

Figure 8: Measured Allan deviation for the zero-rate output of the AOG compared with SAWG.

expected range due to optical alignment variations. The transducer mean scale factor is extracted to be 0.027 µV/(deg/sec).

The zero-rate output (ZRO) of the AOG was recorded for 4 hours and its Allan deviation is plotted in Figure 8 from where we can extract an angular random walk (ARW) of $60^o/\sqrt{hr}$. The figure also compares the noise performance of the AOG with the same gyroscope, but operated as a SAWG with acousto-electrical sensing. The results highlight the better stability of the AOG due to the decoupling between the acoustic drive signal and the optical sensing signal.

ACKNOWLEDGEMENTS

This material is based upon work supported by the DARPA PRIGM-AIMS program under Award No. N66001-16-1-4025. Any opinions, findings, and conclusions or recommendations expressed in this publication are those of the author(s) and do not necessarily reflect the views of DARPA.

REFERENCES

[1] D. M. Rozelle, "The hemispherical resonator gyro: From wineglass to the planets," *Spacefl Mech 2009*, p. 6446.

[2] A. Shebl *et al.*, "Ring laser gyroscope based on standard single-mode fiber and semiconductor optical amplifier," in *2016 33rd National Radio Science Conference (NRSC)*, 2016, pp. 368–376.

[3] Z. Luo, X. Wang, M. Jin, and S. Liu, "MEMS gyroscope yield simulation based on Monte Carlo method," in *2012 IEEE 62nd Electronic Components and Technology Conference*, 2012, pp. 1636–1639.

[4] S. Askari, M. H. Asadian, K. Kakavand, and A. M. Shkel, "Vacuum sealed and getter activated MEMS Quad Mass Gyroscope demonstrating better than 1.2 million quality factor," in *2016 IEEE International Symposium on Inertial Sensors and Systems*, 2016, pp. 142–143.

[5] A. Mahmoud, W. Fikry, Y. M. Sabry, and M. A. E. Mahmoud, "Staggered mode MEMS gyroscope," in *2016 Fourth International Japan-Egypt Conference on Electronics, Communications and Computers (JEC-ECC)*, 2016, pp. 103–106.

[6] M. S. Weinberg and A. Kourepenis, "Error sources in in-plane silicon tuning-fork MEMS gyroscopes," *J. Microelectromechanical Syst.*, vol. 15, no. 3, pp. 479–491, Jun. 2006.

[7] M. Kurosawa, Y. Fukuda, M. Takasaki, and T. Higuchi, "A surface-acoustic-wave gyro sensor," *Sens. Actuators Phys.*, vol. 66, no. 1, pp. 33–39, Apr. 1998.

[8] M.Mahmoud, L.Cai, C.Bottenfield, and G.Piazza, "Fully Integrated Lithium Niobate Electro-Optic Modulator based on Asymmetric Mach-Zehnder Interferometer Etched in LNOI Platform," presented at the IEEE photonics, 2017.

[9] H. Oh, W. Wang, S. Yang, and K. Lee, "Development of SAW based gyroscope with high shock and thermal stability," *Sens. Actuators Phys.*, vol. 165, no. 1, pp. 8–15, Jan. 2011.

[10] M. Mahmoud, S. Ghosh, and G. Piazza, "Lithium Niobate on Insulator (LNOI) Grating Couplers," in *CLEO: 2015 (2015), paper SW4I.7*, 2015, p. SW4I.7.

[11] NANOLN JINAN Jingzheng 超平硅片 超平石英片 .: http://www.nanoln.com/en/

CONTACT

*A Mahmoud, tel: +1-412-8808461; ashrafm@andrew.cmu.edu

†Equal contributions.